Pergamon

Int. J. Heat Mass Transfer. Vol. 39, No. 12, pp. 2505–2514, 1996

0017–9310/96 $15.00 + 0.00

0017–9310(95)00319–3

Prediction of turbulent heat transfer in rotating smooth square ducts

SANDIP DUTTA
Department of Mechanical Engineering, University of South Carolina, Columbia, SC 29208, U.S.A.

and

MALCOLM J. ANDREWS and JE-CHIN HAN
Department of Mechanical Engineering, Texas A&M University, College Station, TX 77843-3123, U.S.A.

(*Received* 19 *January* 1995 *and in final form* 14 *August* 1995)

Abstract—A two-equation turbulence model with new terms for Coriolis and rotational buoyancy has been used for prediction of heat transfer from the leading and trailing sides of a rotating square channel with radially outward flow. Test cases with different Reynolds, Grashof, and rotation numbers are considered. Modeling terms for the Coriolis and buoyancy effects in the k and ε transport equations are shown to give predictions that are in better agreement with the experimental data. Flow separation at the leading wall is found to enhance heat transfer. The mechanism of flow separation is explained with a non-dimensional parameter that characterizes an adverse buoyancy force. Copyright © 1996 Elsevier Science Ltd.

1. INTRODUCTION

Advanced turbine blades require sophisticated cooling techniques to withstand high levels of mechanical stress in an elevated temperature environment. Flow and related heat transfer in a rotating channel are of interest to engineers to understand and improve internal cooling of turbine blades. However, flow in a rotating frame is complex and three-dimensional due to the presence of Coriolis and centrifugal forces. A strong temperature gradient, if present, creates a centrifugal buoyancy effect that causes complex secondary flow patterns and consequently modifies heat transfer coefficients. Due to the complexity of instrumentation in a rotating duct there is little experiment data for velocity measurements and most reported results are in unheated ducts [1].

Most earlier numerical work about rotating ducts used either simple flow models (some of them inviscid models) or parabolic methods for unheated ducts. In particular Majumdar *et al.* [2] showed that parabolic predictions with the standard k–ε model are not satisfactory for moderate to high rotation numbers, Ro, and suggested the need for modifications to account for the rotational effects. Later, Howard *et al.* [1] used Coriolis modified turbulence models and improved the predictions of fully developed rotating mean flow and turbulent viscosity. Launder *et al.* [3] developed a second-moment closure turbulence model and satisfactorily predicted rotating fully developed flow without heat transfer. Recent work for heated ducts by Prakash and Zerkle [4] and Tekriwal [5] included thermal buoyancy effects in the momentum and predicted heat transfer results with a high-Reynolds number k–ε model obtaining reasonable qualitative agreement with experimental profiles of local Nusselt numbers. However, trailing wall Nusselt number was significantly underpredicted. Low-Re k–ε model predictions by Tekriwal [6] showed satisfactory results for Nusselt numbers at the leading wall with lower Reynolds number flows ($Re \leqslant 5000$) but the predictions were again not satisfactory at the trailing wall.

Improvements in the prediction of internal cooling in rotating ducts has evolved through various stages; Dutta *et al.* [7] improved on the heat transfer predictions of Prakash and Zerkle [4] by including a Coriolis turbulence production term from Howard *et al.* [1]. Dutta *et al.* [7] compared PZ and Coriolis modified models for smooth entrance conditions. Encouraged by the results reported in Dutta *et al.* [7], the model has been extended to predict other features of heated rotational flows. This paper describes our work to consider the effects of rotational buoyancy on heat transfer. The centrifugal buoyancy level in the fluid is varied by changing wall temperatures while all other parameters remain fixed. Unlike previous publications, this paper measures the buoyancy level by Grashof number instead of a density ratio. We have found that flow separation due to rotational buoyancy is well explained with a Grashof/Reynolds number ratio that is shown to be the buoyancy counterpart to a Pohlhausen boundary layer parameter. For comparison purposes our simulations

NOMENCLATURE

D, R	Hydraulic diameter of the channel, mean rotating radius of the heated duct
Gr	Grashof number: $Gr = -\rho^2\Omega^2 R\beta(T_w - T_{in})D^3/\mu^2$
Gr/Re	Overall duct Gr-to-Re ratio: $Gr/Re = -\rho\Omega^2 R\beta(T_w - T_{in})D^2/w_0\mu$
$(Gr/Re)_{local}$	Local turbulent Gr-to-Re ratio: $(Gr/Re)_{local} = -\rho\Omega^2 z\beta(T - T_{in})D^2/\lvert w\rvert(\mu+\mu_t)$
h, K_{air}	Convective heat transfer coefficient, thermal conductivity of air
k, ε	Turbulent kinetic energy and its dissipation rate
Nu	Nusselt number: $Nu = hD/K_{air}$
Nu^*, Nu_0	Nu, turbulent fully developed pipe flow: $Nu^* = 0.022Re^{0.8}Pr^{0.6}$, $Nu_0 = 0.023Re^{0.8}Pr^{0.4}$
Pr_t, Pr	Turbulent and laminar Prandtl numbers: $Pr_t = 0.9$, $Pr = 0.72$
Re, Ro	Reynolds number: $Re = \rho w_0 D/\mu$, Rotation number: $Ro = \Omega D/w_0$
T_w, T_{in}	Wall temperature and inlet air temperature
u, v, w	Velocities in x, y and z directions
$\mathbf{U}, z_0$	Velocity vector, distance measured from the start of heating along z
$w_0, \lvert w\rvert$	Average velocity through the duct and absolute local axial velocity.

Greek symbols

β	Volume expansion coefficient
μ_t, μ	Turbulent and laminar viscosity
Ω, ρ	Rotational speed, density of air.

Turbulence models

PZ	Model of Prakash and Zerkle [4]: Coriolis and buoyancy in momentum equations
CB	Coriolis and buoyancy effects in momentum and turbulence generation.

are for the experimental data of Wagner *et al.* [8], and Han and Zhang [9]. These two experiments are well documented and previous numerical workers [4–7] have used these data to judge their model performance. Our model is described next and is followed by results from numerical solutions of the model equations.

2. MATHEMATICAL MODEL

Figure 1 shows the flow and rotation geometry. The following governing equations are based on a coordinate system rotating with the duct. The continuity equation is:

$$\nabla\cdot(\rho\mathbf{U}) = 0 \tag{1}$$

and the momentum equations are

$$\nabla\cdot(\rho u\mathbf{U} - \mu_{eff}\nabla u) = -\frac{\partial\left(p - \frac{\rho\Omega^2 r_x^2}{2}\right)}{\partial x} - 2\rho\Omega w - \rho\Omega^2 r_x\beta(T - T_{in}) + S^u \tag{2}$$

$$\nabla\cdot(\rho v\mathbf{U} - \mu_{eff}\nabla v) = -\frac{\partial p}{\partial y} + S^v \tag{3}$$

$$\nabla\cdot(\rho w\mathbf{U} - \mu_{eff}\nabla w) = -\frac{\partial\left(p - \frac{\rho\Omega^2 r_z^2}{2}\right)}{\partial z} + 2\rho\Omega u - \rho\Omega^2 r_z\beta(T - T_{in}) + S^w \tag{4}$$

where $\mathbf{U}$ is the velocity vector (u, v, w).

The second and third terms on the right-hand side in the x and z momentum equations, (2) and (4), represent Coriolis and rotational buoyancy forces, with rotation radii r_x and r_z in x and z directions (see Fig. 1). The source terms, S^u, S^v and S^w are Boussinesq approximations of the turbulent stresses. Since there is no abrupt change in the flow area, the S^u, S^v and S^w source terms are negligible when compared with the other components of the momentum equations and, as in [4] and [5] are not included in the present predictions. The effective viscosity, μ_{eff}, includes laminar, μ, and turbulent viscosities, μ_t, as

$$\mu_{eff} = \mu + \mu_t; \quad \mu_t = \rho C_\mu \frac{k^2}{\varepsilon}. \tag{5}$$

The enthalpy, i, transport equation is

$$\nabla\cdot(\rho i\mathbf{U} - \Gamma_i\nabla i) = 0; \quad \Gamma_i = \frac{\mu}{Pr} + \frac{\mu_t}{Pr_t}. \tag{6}$$

The k and ε transport equations are

$$\nabla\cdot(\rho k\mathbf{U} - \frac{\mu_t}{\sigma_k}\nabla k) = P - \rho\varepsilon + P_c + P_b \tag{7}$$

$$\nabla\cdot(\rho\varepsilon\mathbf{U} - \frac{\mu_t}{\sigma_\varepsilon}\nabla\varepsilon) = (C_1 P + P_c + C_3 P_b)\frac{\varepsilon}{k} - C_2\rho\frac{\varepsilon^2}{k} \tag{8}$$

where P is the usual Reynolds stress turbulence production term [7]. The buoyancy and Coriolis gen-

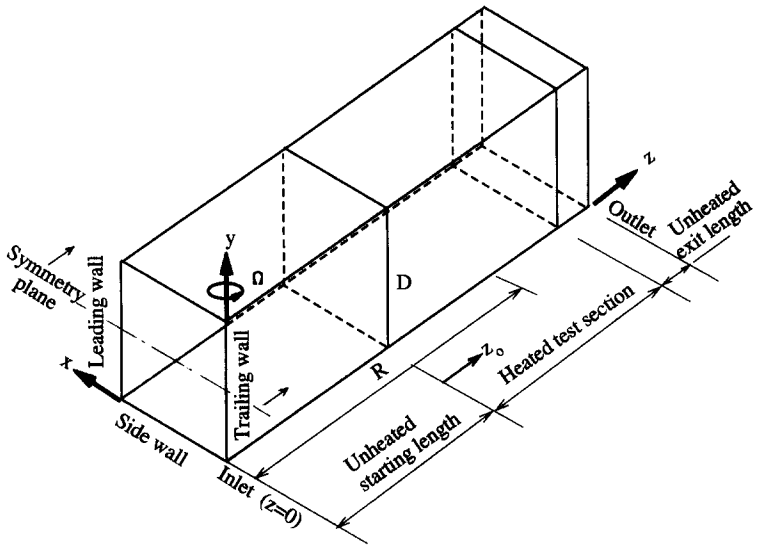

Fig. 1. Physical configuration and coordinate system (not to scale).

erated turbulence production terms, P_b and P_c, are taken as

$$P_b = \frac{\mu_t}{Pr_t}\beta\Omega^2 r_z \frac{\partial T}{\partial z}; \quad P_c = 9\Omega\mu_t \frac{\partial w}{\partial x}. \tag{9}$$

The buoyancy production term, P_b, and the related constant $C_3 = 0.9$ are due to Snider and Andrews [10]. This P_b term arises from a Boussinesq approximation of the velocity–temperature cross-correlation [11]. The Coriolis modified term, P_c, is included from Howard *et al.* [1]. In general, P_c is positive near the trailing wall and negative near the leading wall. A positive P_c increases turbulence and a negative P_c suppresses turbulence. The boundary layer velocity profile near the wall means that P_c has a stronger influence at the near wall region than P_b for the flow and heat transfer situations to be considered. We have found that P_b has less than a 5% influence on heat transfer for radial outward flow. However, P_b is retained for completeness, and may have a significant contribution in the future heat transfer prediction for the turn region in a two-pass duct (one pass with radial outward flow and the other pass with radial inward flow [9]). P_c and P_b were not included in the k–ε models used by previous workers, particularly Prakash and Zerkle [4] hereafter referred to as the PZ model. The other model constants have the following values [12]: $\sigma_k = 1.0$, $\sigma_\varepsilon = 1.314$, $C_\mu = 0.09$, $C_1 = 1.44$ and $C_2 = 1.92$. The Coriolis and buoyancy modified turbulence model as described by equations (7)–(9) will be referred to as CB model in later sections of this paper.

To obviate the need for a fine grid at the wall the CB model uses a wall function approach, and this also means less computation effort than a low Reynolds number k–ε model or an algebraic turbulence model. Near wall nodes use the non-equilibrium wall function of Launder and Spalding [12]. Rosten and Worrell [13], and Dutta *et al.* [7] give the detailed equations for the generalized non-equilibrium wall function.

3. REVIEW OF EXPERIMENTS USED FOR COMPARISON

Two experiments have been used to test the model. One is from Wagner *et al.* [8] and the other is from Han and Zhang [9]. The channel cross-section for both cases is 12.7 mm × 12.7 mm. Table 1 lists other geometrical features and flow parameters.

Wagner *et al.* [8] experimented in a pressurized channel (working pressure of 10 atm = 10^6 N m^{-2}), air properties at that pressure are used for modeling. Wagner *et al.* [8] had heat transfer results for different Grashof numbers corresponding to different wall temperatures. Three Grashof numbers, corresponding to three different T_w, are chosen for this paper: $Gr = -0.4 \times 10^9$, -0.23×10^9 and -0.12×10^9. The corresponding wall-to-coolant density ratios (density ratio $= (T_w - T_{in})/T_w$) are 0.22, 0.13 and 0.07. These density ratios span the thermal boundary conditions investigated by Wagner *et al.* [8]. We have deliberately defined the Grashof numbers so that a negative value implies rotational buoyancy opposing radial outflow, whereas a positive value implies a driving buoyancy force.

Table 1. Flow and geometrical features of the experiments

Parameter	Wagner *et al.* [8]	Han and Zhang [9]
D	12.7 mm	12.7 mm
R	49D	30D
Heated length	14D	12D
Re	25 000	5000
Ro	0.24	0.176

Table 2. Grashof numbers used by Han and Zhang [9]

Wall heating condition	Trailing wall $Gr(T_w)$	Leading wall $Gr(T_w)$	Side wall $Gr(T_w)$
Case A (Uniform wall temperature)	-0.22×10^7 (60°C)	-0.22×10^7 (60°C)	-0.22×10^7 (60°C)
Case B (Uniform heat flux)	-0.15×10^7 (50°C)	-0.22×10^7 (60°C)	-0.18×10^7 (53°C)

Han and Zhang [9] provided heat transfer results with different wall heating conditions. Table 2 gives the experimental wall heating conditions. Wagner *et al.* [8] studied the heat transfer with uniform wall temperature. In contrast, Han and Zhang [9] included a uniform wall heat flux condition (Case B). These two experiments cover a wide range of Reynolds numbers and buoyancy effects, hence this variety in data form a good basis for the evaluation of the new CB model.

4. NUMERICAL DETAILS

4.1. *General computational details*

As in Dutta *et al.* [7], Prakash and Zerkle [4] and Tekriwal [5] the three-dimensional PHOENICS software package has been used. However, in the present work we have added our own rotational terms [Coriolis and buoyancy terms in momentum equations, and turbulence production terms as in equation (9)] in the governing equations. Inlet conditions were given at the entrance plane of the channel (center of rotation) and uniform profiles were used for all the variables. Figure 1 shows a schematic of the test configuration. The axial w-velocity was assigned from the mean flow rate. The transverse velocities, u and v, were set to zero. Values for k and ε were $k = 0.2\%$ of w_0^2 and $\varepsilon = C_\mu k^{3/2}/D$. The enthalpy at the inlet was calculated based on experimental $T_{in} = 300$ K. To match the experiments of both Wagner *et al.* [8] and Han and Zhang [9] an isothermal fixed temperature boundary condition was used for the heated walls. Unheated walls were thermally insulated with a zero flux boundary condition. Zero gradient, parabolic outflow conditions were applied at the outlet for all the variables solved.

Because of symmetry, the computation domain covered only half the channel in the y-direction. The computational grid was deliberately finer on the trailing side in comparison with the leading side because a substantial drop in kinetic energy and eddy viscosity was found on the leading side with the modified k–ε model [14]. A y^+ value greater than 11.63 is desirable for the wall functions so that the near wall node is in the turbulent boundary layer and not in the laminar sublayer. Like Prakash [15] we found y^+ values for the leading side were less than 10 near the separation region. The turbulence model reverts to the laminar case for $y^+ < 11.63$.

Grid independence tests similar to Dutta *et al.* [7] and Tekriwal [5] were performed. Three sets of grids were tested for grid independence: $10\times5\times55$, $15\times8\times55$ and $15\times8\times80$. It was found that heat transfer and flow predictions varied by 5% and 8% with this grid selection. All the results presented in this paper are for a grid of $15\times8\times55$. A mass residue of less than 10^{-6} was taken to be the convergence criteria; however, spot values of all the variables were monitored and less than 0.5% variation was observed in the last 50 iterations.

4.2. *Simulation details for the experiments of Wagner* et al. [8]

The experimental setup of Wagner *et al.* [8] had a screened plenum chamber at the inlet of the heated rotating test section. McGrath and Tse [16] showed that this inlet plenum has a significant effect on the velocity distribution. We have taken a different approach from that of McGrath and Tse [16]. Instead of physically defining the plenum, we have modeled it in terms of a non-dimensional parameter. The plenum chamber has a larger hydraulic diameter ($\approx 1.5D$) and therefore a smaller axial flow velocity ($\approx 0.4w_0$) than the heated section of the duct. Dutta *et al.* [17] discussed this inlet condition in detail and showed that to simulate the entrance rotation number, the flow needs to be maintained at $4Ro$ ($\Omega^*1.5D/0.4$ $w_0 = 3.75Ro \approx 4Ro$) before the flow enters the heated section. This inlet condition was included in our CB model simulations. The CB model predictions also included enhancement of turbulence by the Coriolis effect (positive P_c) in the unheated portion of the duct. Dutta *et al.* [7] showed that the modified model laminarizes the leading side and underpredicts the leading side heat transfer. Complete laminarization perhaps cannot be achieved experimentally in rotating rigs because of the inherent vibration. Hence, in the implementation of our CB model for $Re = 25\,000$ and $Ro = 0.24$, the Coriolis modifications to the k–ε transport equations were not applied to the near wall nodes of the leading surface. Moreover, the SIMPLE-SIMPLER family of Navier–Stokes equation solvers are known to be unstable at high Grashof numbers [18] and rotation numbers [19]. Therefore, care was taken to obtain a tight convergence of the numerical solution. We found this was important to ensure a two-vortex solution in agreement with [20]. A typical inertial relaxation time step [21] was 6.7×10^{-5}. Air properties used for modeling were: $\rho = 11.8$ kg m^{-3} and $\mu = 1.9\times10^{-5}$ kg m^{-1} s^{-1}.

4.3. *Simulation details for the experiment of Han and Zhang* [9]

The experimental setup of Han and Zhang [9] did not have a plenum chamber, and the flow was allowed to develop through an unheated duct without any special modeling. The Reynolds number modeled was $Re = 5000$. A typical inertial relaxation time step was 2.3×10^{-5} and air properties were: $\rho = 1.18$ kg m^{-3} and $\mu = 1.9 \times 10^{-5}$ kg m^{-1} s^{-1}.

5. RESULTS AND DISCUSSION

5.1. *Comparison with Wagner* et al. [8]: *effect of Grashof number*

Wagner *et al.* [8] showed that rotation for a radially outward flow condition increases the Nusselt number on the trailing side and decreases the Nusselt number on the leading side. Isotherm profiles of the flow change with an alteration in the wall temperature. This variation of temperature in the rotating flow changes the heat transfer patterns in the presence of a centrifugal buoyancy force. This effect is related to the free convection along a vertical heated wall, and so has been characterized with a Grashof number (Gr). Three Grashof numbers have been selected for comparison with our CB model: $Gr = -0.4 \times 10^9$, -0.23×10^9 and -0.12×10^9.

Figure 2 shows the Nusselt number predictions by the PZ and our CB model. The plotted Nusselt number ratios are averaged across the respective walls in the y-direction. The trailing side heat transfer is underpredicted and the leading side heat transfer is acceptably predicted by the PZ model [4]. The extended k–ε model predictions of Tekriwal [5] are similar to the PZ model predictions of Prakash and Zerkle [4]. However, Prakash and Zerkle [4] and Tekriwal [5] did not include the effects from the upstream plenum chamber. Figure 2 shows that our CB model prediction is significantly better for the trailing wall than the PZ model. The comparatively high trailing side heat transfer prediction by the PZ model relative to that on the leading side is primarily due to a four-

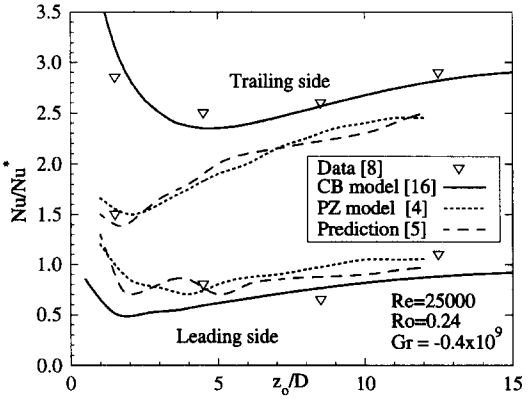

Fig. 2. Comparison of predicted surface averaged local Nusselt number distributions by different k–ε models.

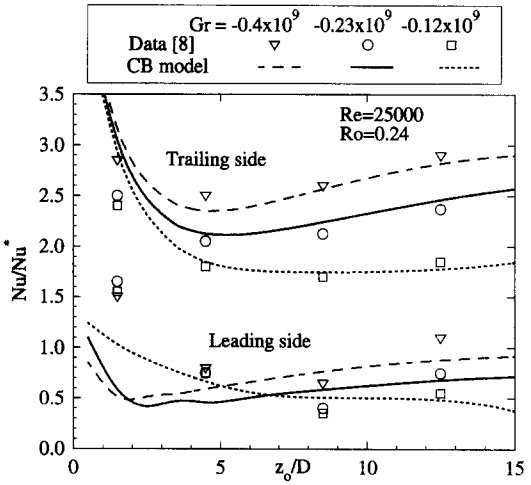

Fig. 3. Nusselt number predictions by the CB model.

vortex secondary flow prediction, in which there are two smaller vortices near the trailing wall and these smaller secondary flow vortices increase heat transfer from the trailing wall. Whereas, the CB model predictions have a two-vortex structure and an asymmetric distribution of turbulence. The CB model prediction of the trailing wall heat transfer enhancement is mostly by an increase in turbulence by rotational effects and is consistent with the experimental flow observations [19].

Figure 2 shows that predictions by PZ and CB models at the leading wall are comparable with an increase in Nusselt number at downstream locations. This increase in Nusselt number is due to the rotational buoyancy [third term on the right-hand side of equation (4)] that opposes the flow near hot walls. Consequently it is more active near the hotter leading wall, where there is a lower air flow rate. Ultimately this adverse rotational buoyancy force causes the flow to separate at the leading wall. The turbulence level and thus heat transfer increase downstream of the separation location. Figure 3 shows the CB k–ε model predictions of heat transfer for three Grashof numbers. The CB model predictions are in good agreement with the experimental data. Both experiment and predictions show that the heat transfer increases with an increase in rotational buoyancy effect.

Figure 4 shows vector plots of secondary flow patterns and contours of the axial flow velocity predicted by the CB k–ε model for the highest and lowest Grashof numbers. Figure 4 reveals that in rotation, the core flow shifts toward the trailing side. The CB k–ε model shows two vortex structures (one on each side of the symmetry plane). In contrast, Dutta *et al.* [7] predicted a four vortex structure with the PZ model. The current model predicts higher turbulence near the trailing wall and dissipates the smaller vortex to form a single dominant vortex in each half of the square channel. The flow with stronger rotational buoyancy (more negative Grashof number) separates at the

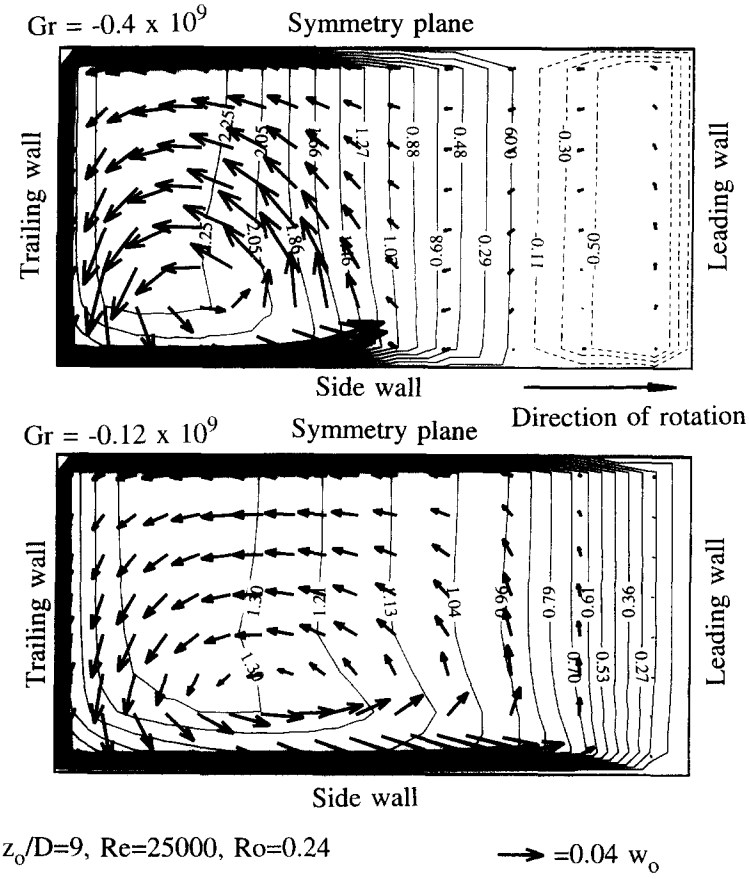

Fig. 4. CB model predictions of secondary flow vectors and w/w_0 contours.

leading wall. The flow separation mechanism is depicted in Fig. 5. Since the Coriolis force is zero at the no-flow stagnation point, the Coriolis force alone cannot create a flow separation. In the separated region the Coriolis force acts towards the leading wall to promote a collapse of the separation bubble. Hence the Coriolis force does not favor a flow separation. This balance between buoyancy and Coriolis is discussed in more detail later in this section.

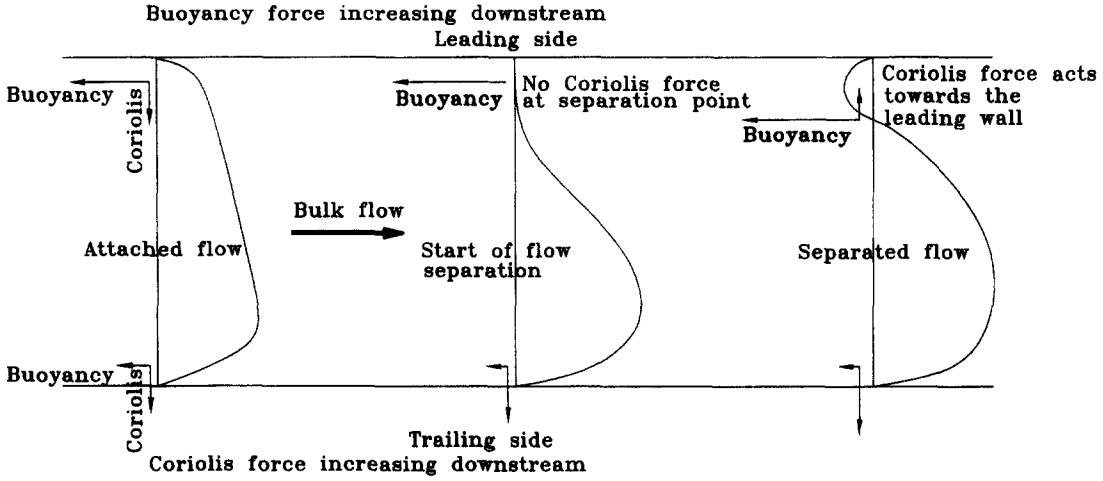

Fig. 5. Schematic of the flow separation mechanism at the leading wall.

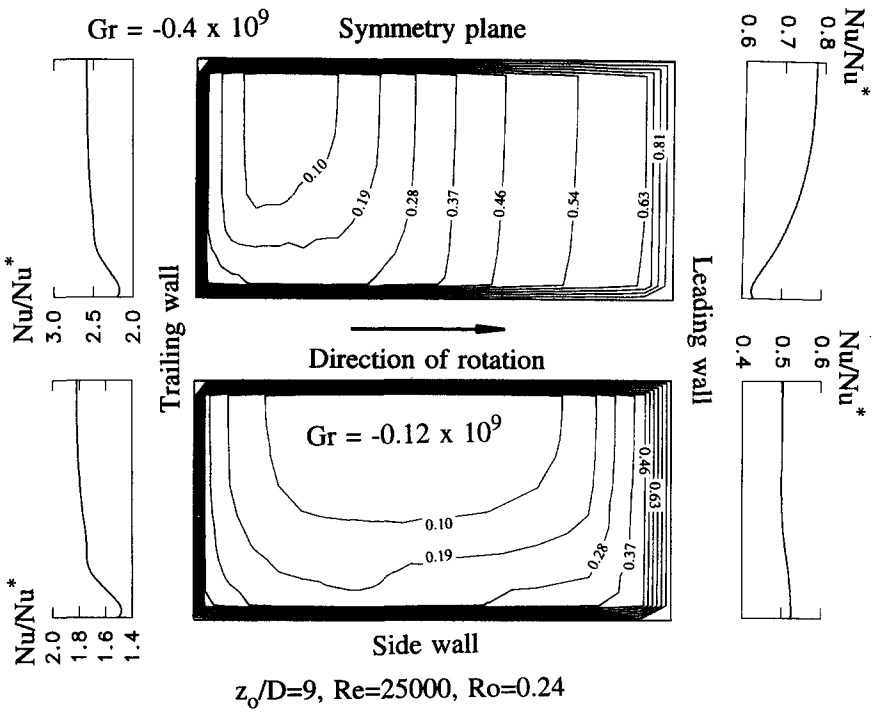

Fig. 6. CB model predictions of $(T-T_{in})/(T_W-T_{in})$ contours and local Nusselt number ratio profiles.

Figure 6 shows isotherms for the two heating conditions. Due to flow separation and slower fluid movement near the leading wall, for $Gr = -0.4\times10^9$, the temperature rise of the fluid at the leading wall is higher than that for $Gr = -0.12\times10^9$. Figure 6 also shows the local Nusselt numbers at the leading and trailing surfaces.

Figure 7(a)–(c) compare flow related quantities: axial velocity, turbulent eddy viscosity, and local Grashof/Reynolds number ratio, predicted by the CB model at Grashof numbers of -0.4×10^9 and -0.12×10^9. The predictions are at the centerline $(y/D = 0.5)$ for different radial locations (z_0/D). The axial velocity of Fig. 7(a) shows that at the stronger Grashof number the flow separates near the leading wall and because of mass conservation the flow velocity near the trailing wall increases. The Coriolis force opposes the separation process and counteracts the rotational buoyancy force in the reversed flow (see Fig. 5). A balance of these two forces and an increased eddy viscosity in the bulk flow make the separation region stable and no significant growth rate is observed at down stream locations.

Figure 7(b) shows the predicted eddy viscosity profiles. Johnston *et al.* [20] experimentally observed suppression of turbulence near the leading side for an unheated duct. This experimental observation supports the laminarization predicted by the CB model in Fig. 7(b). Figure 7(b) shows near absence of turbulent eddy viscosity for attached low buoyant flow $(Gr = -0.12\times10^9)$. Flow separation causes a steeper gradient in the velocity profile resulting in an increase of eddy viscosity at the separation bubble. The eddy viscosity of the core flow for $Gr = -0.4\times10^9$ increases at downstream of $z_0/D = 5.4$ due to the buoyancy generated turbulence. A high eddy viscosity at the core flow makes the velocity distribution linear with x [see Fig. 7(a)].

Figure 7(c) shows the local turbulent Grashof/Reynolds number ratio, $(Gr/Re)_{local}$, that is based on the local temperature, turbulent eddy viscosity, and flow rate. The overall duct Grashof/Reynolds number ratios $(Gr/Re = -\rho\Omega^2R\beta(T_W-T_{in})D^2/w_0\mu)$ are: -16000, -9200 and -4800 for the three wall temperatures. Whereas the order of magnitude of peak $(Gr/Re)_{local}$ is -1000 to -5000. The difference is associated with the lower local temperature difference and higher local eddy viscosity. The Grashof/Reynolds number ratio is a measure of the balance between adverse buoyancy and boundary layer momentum. Formulation of this ratio is similar to the Pohlhausen parameter [22] used as a flow separation criterion in aerodynamics where the usual adverse pressure gradient has been replaced by an adverse buoyancy effect. The $-(Gr/Re)_{local}$ shows a peak at the edge of the flow reversal. This peak is due to near zero axial velocity at the edge of the flow reversal where the transition from negative to positive velocities occur [see Fig. 7(a)].

5.2. *Comparison with Han and Zhang* [9]: *effect of wall heating conditions*

Table 2 lists the wall heating conditions used by Han and Zhang [9]. The Grashof numbers are smaller

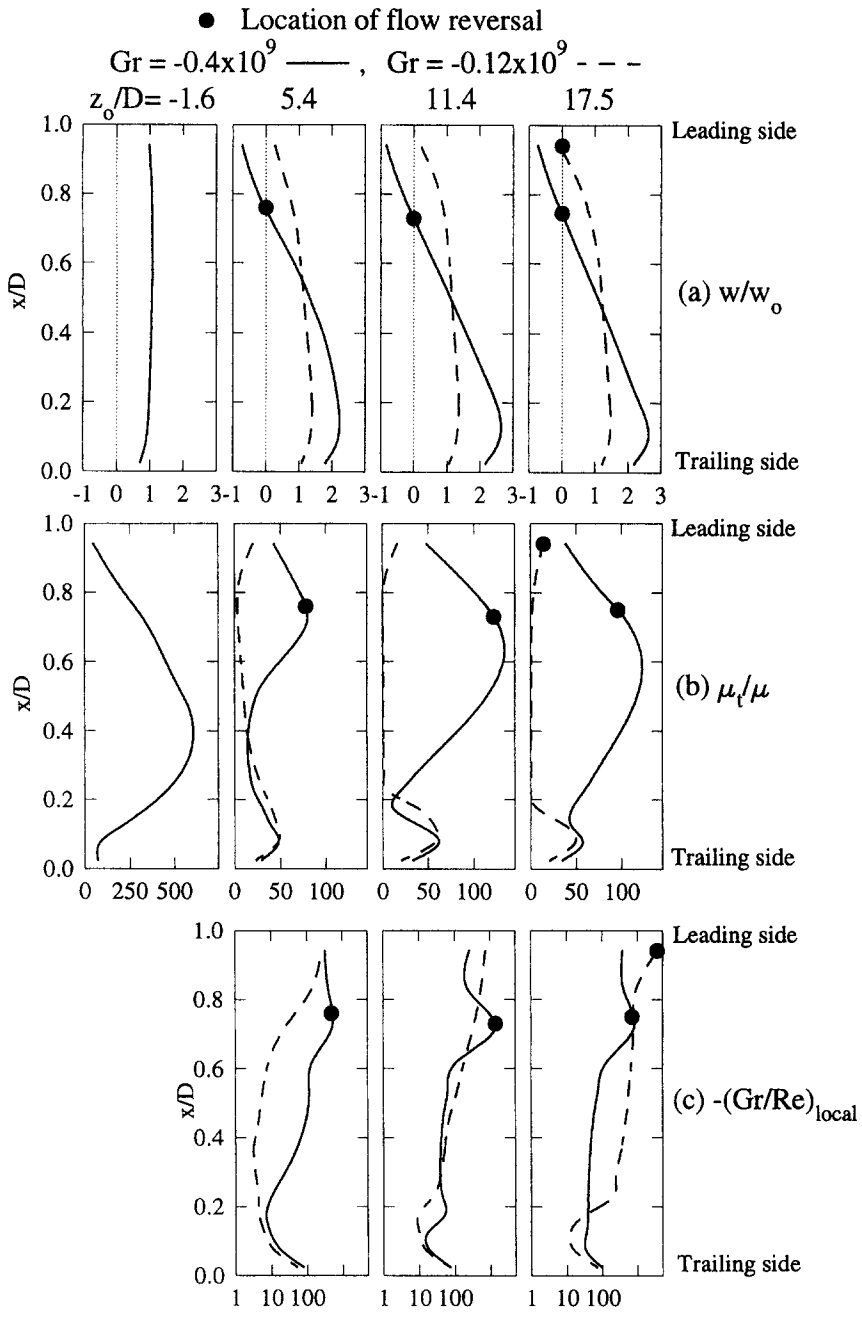

Fig. 7. Flow related predictions by the CB model for $Re = 25\,000$ and $Ro = 0.24$ at $y/D = 0.5$.

(-0.22×10^7) than those of Wagner *et al.* [8]. The predictions do not indicate flow separation with this Grashof/Reynolds number ratio ($Gr/Re = -440$ for Case A). Unlike Wagner *et al.* [8], Han and Zhang [9] varied the temperatures of the adjacent walls and noticed a significant effect on the Nusselt numbers. Figure 8 compares PZ and CB k–ε model predictions for leading and trailing wall Nusselt numbers with the experimental data with the heating condition of Case A as given in Table 2. Figure 8 shows that the present CB model gives better agreement with the data than the PZ model. Improvements in the CB model predictions are due to the inclusion of rotational turbulence generation terms.

Figure 9 presents the predicted and measured Nusselt number ratios for Cases A and B. Case A is a uniform wall temperature boundary condition and Case B is similar to a uniform wall heat flux condition. Thermal boundary conditions for Cases A and B are given in Table 2. The CB model predictions show that, unlike experiment, the heating condition does not influence the heat transfer significantly for the flow situation considered. The inlet bulk temperatures were corrected by 4°C and 6°C based on the actual exper-

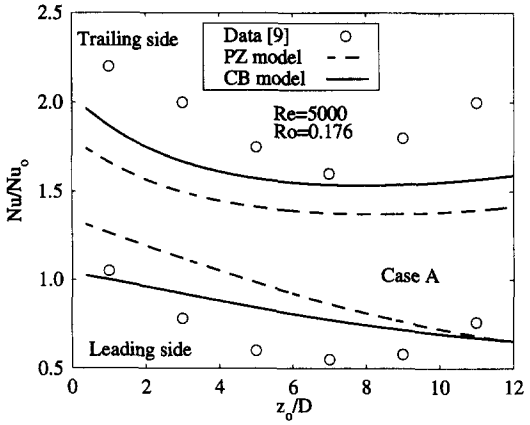

Fig. 8. Comparison of PZ and CB model predictions.

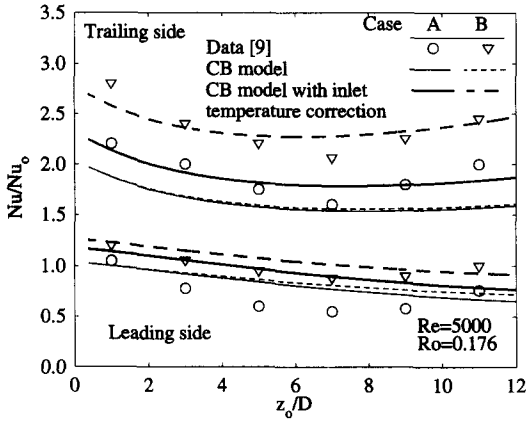

Fig. 9. Surface averaged Nusselt number predictions for Cases A and B.

imental conditions for Cases A and B, respectively, giving satisfactory agreement with the experimental data. However, at this relatively low Reynolds number ($Re = 5000$) both the experimental data and predictions suffer from uncertainty because of low Reynolds number turbulent flow.

Figure 10 shows a vector plot of the secondary flow superimposed on the axial flow contour plot. Results for Case A are displayed, Case B is similar. The Coriolis and rotational buoyancy forces shift the axial flow toward the trailing side. However the Grashof/Reynolds number ratio is not strong enough to cause flow separation near the leading wall.

5.3. *A correlating parameter for flow separation*

The governing equations show that three dominant forces influence the heat transfer and flow in a rotating duct. These three forces are: rotational (buoyancy and Coriolis), inertia, and viscous forces. The established nondimensional parameters, namely Reynolds number, Grashof number, and rotation number (inverse of Rossby number) are based on the balance of two forces. Reynolds number is the ratio of inertia to viscous forces, Grashof number is the ratio of buoyancy to viscous forces, and rotation number is the ratio of Coriolis to inertia forces. To show the influence of three forces, the non-dimensional numbers need to be combined. Wagner *et al.* [8] developed a buoyancy parameter $= Gr/Re^2 = \Omega^2 R\beta(T_w - T_{in}) D/w_0^2$, which neglects the viscous effects and is a Richardson number as defined by Snider and Andrews [23] for natural buoyant mixing. This buoyancy parameter does not include the boundary layer effect. Our investigation recommends the ratio of Grashof number to Reynolds number ($Gr/Re = -\rho\Omega^2 R\beta(T_w - T_{in})D^2/w_0\mu$). This duct Gr/Re ratio includes the rotational, inertia and viscous forces and has been found to be a good parameter to identify the occurrence of flow separation at the leading wall and hence enhancement of heat transfer at downstream locations. Evaluation of Wagner *et al.*'s [8] data shows that duct Gr/Re should be more negative than -2500 to obtain flow separation at the leading wall.

6. CONCLUSIONS

The following conclusions are drawn from this work. The trailing side Nusselt number of a rotating

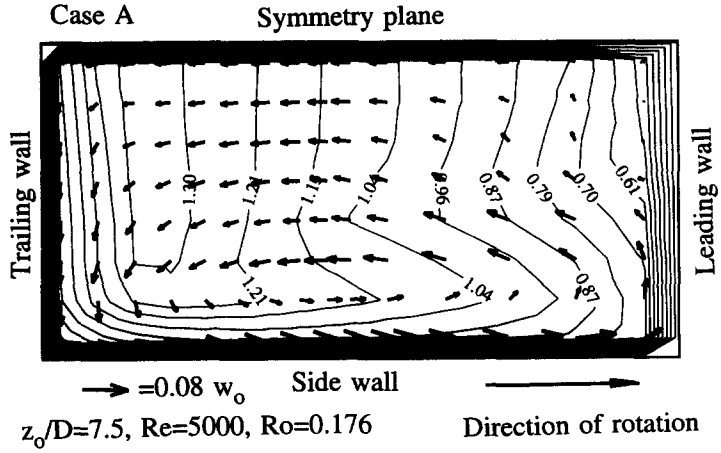

Fig. 10. CB model prediction of secondary flow vector and w/w_0 contour.

duct is higher than the leading side Nusselt number. Satisfactory predictions have been achieved by the inclusion of modeled rotational turbulence generation terms in the momentum and k–ε transport equations. The heated test sections are short resulting in a developing buoyancy dominated flow. The unheated flow section upstream of the heated test section forms a fully developed rotating duct flow. However, the heated section is too short to form a buoyancy induced developed flow. So, consequently, measurements and predictions in the heated duct are affected by the flow developed in the unheated section. A careful re-evaluation of the experimental data from Han and Zhang [9] gave an improved estimate for the inlet temperature that in turn resulted in improved predictions. A more negative Grashof number develops a stronger vortex in the trailing half of the square duct, and as a result the trailing side heat transfer increases. The axial flow separates at the leading surface in the presence of a strong adverse rotational buoyancy force as evidenced by more negative local Grashof-to-Reynolds number ratio $(Gr/Re)_{\text{local}}$ at the location of flow separation. We found the duct Gr/Re ratio to be a useful indicator of leading side flow separation for the heated ducts. Leading side flow separation is estimated to occur at a Gr/Re more negative than -2500. Flow separation enhances the turbulence and consequently heat transfer increases at downstream locations.

Acknowledgements—This work has been possible by a research grant of computer time allocated by the Supercomputing Center, Texas A&M University, College Station, TX.

REFERENCES

1. J. H. G. Howard, S. V. Patankar and R. M. Bordynuik, Flow prediction in rotating ducts using Coriolis-modified turbulence models, *J. Fluids Engng*, **102**, 456–461 (1980).
2. A. K. Majumdar, V. S. Pratap and D. B. Spalding, Numerical computation of flow in rotating ducts, *J. Fluids Engng* **99**, 148–153 (1977).
3. B. E. Launder, D. P. Tselepidakis and B. A. Younis, A second-moment closure study of rotating channel flow, *J. Fluid Mech.* **183**, 63–75 (1987).
4. C. Prakash and R. Zerkle, Prediction of turbulent flow and heat transfer in a radially rotating square duct, *J. Turbomachinery* **114**, 835–846 (1992).
5. P. Tekriwal, Heat transfer predictions with extended k–ε turbulence model in radial cooling ducts rotating in orthogonal mode, *J. Heat Transfer* **116**, 369–380 (1994).
6. P. Tekriwal, Heat transfer predictions in rotating radial smooth channel: comparative study of k–ε models with wall function and low-Re model, ASME Paper No. 94-GT-196 (1994).
7. S. Dutta, M. J. Andrews and J. C. Han, Numerical prediction of turbulent heat transfer in a rotating square duct with variable centrifugal buoyancy effects. In *General Papers in Heat and Mass Transfer, Insulation and Turbomachinery*, ASME-HTD-Vol. 271, pp. 161–170 (1994).
8. J. H. Wagner, B. V. Johnson and T. J. Hajek, Heat transfer in rotating passages with smooth walls and radial outward flow, *J. Turbomachinery* **113**, 42–51 (1991).
9. J. C. Han and Y. M. Zhang, Effect of uneven wall temperature on local heat transfer in a rotating square channel with smooth walls and radial outward flow, *J. Heat Transfer* **114**, 850–858 (1992).
10. D. M. Snider and M. J. Andrews, The simulation of mixing layers driven by compound buoyancy and shear, *J. Fluids Engng* (in press).
11. M. S. Hossain and W. Rodi, A turbulence model for buoyant flows and its application to vertical buoyant jets. In *Turbulent Buoyant Jets and Plumes* (Edited by W. Rodi), pp. 143–146. Pergamon Press, New York (1982).
12. B. E. Launder and D. B. Spalding, The numerical calculation of turbulent flows, *Comput. Meth. Appl. Mech. Engng* **3**(2), 269–289 (1974).
13. H. I. Rosten and J. K. Worrell, Generalized wall functions for turbulent flow, *PHOENICS J.* **1**, 81–109 (1988).
14. S. Dutta, M. J. Andrews and J. C. Han, Heat transfer and flow predictions in a rotating square duct with Coriolis-modified turbulence models, *Heat Transfer* **4**, 219–224 (1994). Presented at the 10th International Heat Transfer Conference, Brighton, England, 14–18 August (1994).
15. C. Prakash, Personal communication, GE-Aircraft Engines, Cincinnati, Ohio (1994).
16. D. M. McGrath and D. G. N Tse, A combined experimental computational study of flow in turbine blade cooling passages: Part II. Numerical simulation. Presented at the 40th Gas Turbine & Aeroengine Congress, Users Symposium & Exposition, 5–9 June, Houston, Texas, ASME Paper No. 95-GT-149 (1995).
17. S. Dutta, M. J. Andrews and J. C. Han, On the simulation of turbulent heat transfer in a rotating duct, *AIAA J. Thermophys. Heat Transfer* **9**(2), 381–382 (1995).
18. J. W. MacArthur and S. V. Patankar, Robust semidirect finite difference methods for solving the Navier–Stokes and energy equations, *Int. J. Numer. Meth. Fluids* **9**, 325–340 (1989).
19. H. Iacovides and B. E. Launder, Parametric and numerical study of fully developed flow and heat transfer in rotating rectangular ducts, *J. Turbomachinery* **113**, 331–338 (1991).
20. J. P. Johnston, R. M. Halleen and D. K. Lezius, Effects of spanwise rotation on the structure of two-dimensional fully developed turbulent channel flow, *J. Fluid Mech.* **56**(3), 533–557 (1972).
21. S. V. Patankar, *Numerical Heat Transfer and Fluid Flow*, p. 68. Hemisphere, New York (1980).
22. F. M. White, *Viscous Fluid Flow*, 2nd Edition, p. 268. McGraw-Hill, Inc., New York (1991).
23. D. M. Snider and M. J. Andrews, Rayleigh–Taylor and shear driven mixing with an unstable thermal stratification, *Phys. Fluids* **6**(10), 3324–3334 (1994).